RSC Advances

PAPER

View Article Online
View Journal | View Issue

Cite this: *RSC Adv.*, 2025, **15**, 12689

A novel ZnO/Fe^{3+}-doped Bi_2WO_6 photocatalyst with triple synergistic effect for solar-driven tetracycline degradation

Hui Sun, Gaoyang Liang, Bingge Chen, Jingqi Jia and Hongxia Jing *

Received 17th March 2025
Accepted 8th April 2025

DOI: 10.1039/d5ra01899d

rsc.li/rsc-advances

To address the limited visible-light absorption and rapid charge recombination of Bi_2WO_6 photocatalysts, this work constructs a Z-scheme ZnO/Fe^{3+}-doped Bi_2WO_6 heterojunction *via* a hydrothermal-calcination method. The Fe^{3+} doping induces the formation of oxygen vacancies and optimizes the band structure, which cooperates with the interface reconstruction of ZnO to expand the light absorption to 480 nm. The hierarchical pore structure simultaneously enhances the mass transfer efficiency, and finally realizes the efficient degradation of tetracycline under visible light (the removal rate is 95.5% in 60 minutes, and the rate is 2.28 times higher than that of the pure phase) and the stable cycle performance is good. Mechanistic studies demonstrate that Z-scheme charge transfer driven by an interfacial built-in electric field ensures effective carrier separation, with photogenerated holes (h^+) as key reactive species. The proposed "defect-heterojunction-interface trinity" strategy establishes a new design scheme for bismuth-based Z-scheme photocatalysts.

1. Introduction

Tetracycline (TC), as a widely used broad-spectrum antibiotic, poses significant challenges for environmental remediation due to its persistent residues and recalcitrant degradation properties.[1–3] Conventional wastewater treatment processes exhibit limited efficiency in TC removal, leading to its continuous accumulation in aquatic environments.[3–6] Moreover, photodegradation byproducts of TC demonstrate enhanced toxicity and bioaccumulation potential, exacerbating ecological risks.[7–9] These limitations highlight the urgent demand for advanced oxidation technologies (AOPs) that enable effective TC degradation while preventing secondary contamination from chemical sludge or toxic intermediates.

Photocatalytic oxidation has emerged as a promising strategy for TC remediation, leveraging solar-driven reactive oxygen species (ROS) generation to achieve contaminant degradation.[10–12] Among various photocatalysts, bismuth tungstate (Bi_2WO_6) has garnered significant attention in visible-light-driven photocatalysis due to its unique layered structure and moderate bandgap (about 2.8–3.0 eV).[13–16] However, pristine Bi_2WO_6 exhibits unsatisfactory photocatalytic TC degradation efficiency (more than 60% under optimal conditions), primarily due to: (1) limited visible-light absorption range ($\lambda <$ 450 nm), which underutilizes 43% of solar spectrum energy; (2) rapid electron-hole recombination, resulting in low quantum efficiency; and (3) insufficient surface active sites for adsorbing TC macromolecules (dimensions: 1.2 × 0.6 nm).[14,17–19] Although modification strategies such as metal ion doping (*e.g.*, Sm^{3+} elevating degradation rate to 80% (ref. 20)) and heterojunction construction (*e.g.*, g-C_3N_4 composites achieving 4-fold rate constant enhancement[21]) show partial success, single-component modifications fail to synergistically address light absorption, charge separation, and substrate adsorption. They face inherent trade-offs in performance and limited performance improvement.

Z-Scheme heterojunctions, inspired by natural photosynthesis, have emerged as a promising strategy to enhance photocatalytic performance. Unlike traditional Type-II heterojunctions, Z-scheme systems enable spatially separated redox reactions by retaining photogenerated electrons and holes with stronger redox potentials. This mechanism not only suppresses charge recombination but also enhances the generation of reactive oxygen species (ROS), such as hydroxyl radicals ($\cdot OH$) and superoxide radicals ($\cdot O_2^-$), which are critical for the degradation of tetracycline. Recent studies have demonstrated that Z-scheme heterojunctions, exhibit superior photocatalytic activity compared to conventional heterojunctions due to their unique charge transfer pathways.[22–24]

This study develops a high-efficiency Bi_2WO_6-based photocatalytic system through synergistic integration of Fe^{3+} doping and ZnO heterojunction engineering. The dual modification of Fe^{3+} and ZnO achieved triple enhancement: broadening spectral response *via* defect engineering, improving charge separation through a Z-scheme pathway, and optimizing TC adsorption-mass transport *via* hierarchical porosity. Mechanistic studies identify photogenerated holes (h^+) as the

School of Chemistry and Chemical Engineering, North University of China, Taiyuan 030051, P. R. China. E-mail: jhx820215@126.com

dominant reactive species, advancing fundamental understanding of charge behavior. Furthermore, the "defect-heterojunction-interface trinity" design framework unifies structural optimization, reaction dynamics control, and system adaptability, establishing a novel paradigm for rationally developing bismuth-based Z-scheme photocatalysts toward complex antibiotic-polluted environments.

2. Experimental

2.1 Materials and methods

All chemicals, including bismuth nitrate pentahydrate ($Bi(NO_3)_3 \cdot 5H_2O$), sodium tungstate dihydrate ($Na_2WO_4 \cdot 2H_2O$), ferric nitrate nonahydrate ($Fe(NO_3)_3 \cdot 9H_2O$), zinc oxide (ZnO), sodium hydroxide (NaOH), anhydrous ethanol, were purchased from Shanghai McLean Biochemical Technology Co., Ltd, and used directly without any further purine cations. Deionized water was obtained using a Milli-Q system (Millipore).

2.2 Preparation of Bi_2WO_6 and Fe^{3+}-Bi_2WO_6

A mixture of 3.880 g $Bi(NO_3)_3 \cdot 5H_2O$ and 1.319 g $Na_2WO_4 \cdot 2H_2O$ was dissolved in 40 mL deionized water. The pH of the solution was adjusted to 4.0 using 0.1 M HNO_3/NaOH, followed by ultrasonication for 30 min. The homogeneous suspension was transferred into a 100 mL Teflon-lined stainless steel autoclave and heated at 180 °C for 24 h in a muffle furnace. After cooling to room temperature, the precipitate was collected by centrifugation (8000 rpm, 10 min), washed three times with ethanol and deionized water, and dried at 80 °C for 12 h. Finally, the Bi_2WO_6 powder was obtained by calcination at 300 °C for 1 h in air.

3.880 g $Bi(NO_3)_3 \cdot 5H_2O$, 1.319 g $Na_2WO_4 \cdot 2H_2O$, and a stoichiometric amount of $Fe(NO_3)_3 \cdot 9H_2O$ (corresponding to Fe^{3+} : Bi_2WO_6 molar ratios of 0.1 : 100, 0.26 : 100, 0.52 : 100, and 0.78 : 100) were dissolved in 40 mL deionized water. The subsequent steps (pH adjustment, ultrasonication, hydrothermal treatment, and calcination) were identical to the synthesis of pristine Bi_2WO_6. The synthesized products were named as 0.1Fe^{3+}-doped Bi_2WO_6, 0.26Fe^{3+}-doped Bi_2WO_6, 0.52Fe^{3+}-doped Bi_2WO_6, and 0.78Fe^{3+}-doped Bi_2WO_6.

2.3 Preparation of ZnO/Fe^{3+}-doped Bi_2WO_6

3.880 g $Bi(NO_3)_3 \cdot 5H_2O$, 1.319 g $Na_2WO_4 \cdot 2H_2O$, 0.010 g $Fe(NO_3)_3 \cdot 9H_2O$ were put into beaker A and 40 ml H_2O was added. A certain amount of ZnO (0.558 g, 1.116 g, 1.674 g, 2.233 g) was put into beaker B and 40 mL H_2O was added. The pH was adjusted to 4 and the ultrasonication for 30 min. The above samples were mixed ultrasonically until they were mixed evenly, transferred to the reactor and put into the oven at 180 °C for 24 h. After cooling to room temperature, the precipitate was collected by centrifugation. Then the sample ZnO/Fe^{3+}-doped Bi_2WO_6 was obtained by calcining at 300 °C for 1 h.

2.4 Characterization

The crystal structure of the synthesized samples was characterized using a Rigaku Miniflex-600 X-ray diffractometer (XRD). The optical absorption properties and bandgap energy were determined by Shimadzu UV-2600 UV-vis diffuse reflectance spectroscopy (UV-DRS). Chemical bonding and functional groups were analyzed with a Shimadzu FTIR-8400S Fourier transform infrared spectrometer (FT-IR). The surface morphology and microstructure were examined using a TESCAN MIRA LMS field-emission scanning electron microscope (FE-SEM). High-resolution transmission electron microscopy (HRTEM) analyse was conducted on a JEOL JEM-F200 transmission electron microscope (TEM). The Brunauer–Emmett–Teller (BET) specific surface area and pore size distribution were measured with a Micromeritics ASAP 2460 four-station physisorption analyzer. Surface chemical states were investigated *via* Thermo Scientific K-Alpha X-ray photoelectron spectroscopy (XPS). Electrochemical properties, including electrochemical impedance spectroscopy (EIS), transient photocurrent response (TPC), and Mott–Schottky analysis, were evaluated using a Bio-Logic VSP-300 electrochemical workstation.

2.5 Photodegradation experiments

To mimic solar irradiation, a 250 W metal halide lamp was employed. The photocatalytic performance of the synthesized material was evaluated by monitoring the degradation of TC in an aqueous solution. The specific operation is as follows: 75 mg of the prepared powder sample was mixed with 100 mL of 10 mg per L tetracycline aqueous solution in a 150 mL beaker, and then stirred for 30 min in a dark environment to achieve adsorption equilibrium. After the dark reaction, it was placed under a simulated light source, and the light began to be timed, and 5 mL of the mixture was taken every 15 min. Following centrifugation, the supernatant was carefully decanted, and the absorbance of the TC solution was determined at a wavelength of 357 nm. Photocatalytic activity was quantified by assessing the degree of TC degradation in the solution. The degradation efficiency (η) was calculated using the following equation:

$$\eta = [(A_0 - A_t)/A_0] \times 100\% \quad (1)$$

Additionally, experiments were carried out to identify the primary reactive species involved in the photocatalytic process.

In the experiment, isopropyl alcohol (IPA) was introduced as a scavenger for hydroxyl radicals ($\cdot OH$), and 1,4-benzoquinone (BQ) for superoxide radicals ($\cdot O_2^-$), and ethylenediaminetetraacetic acid disodium salt (EDTA-2Na) for photogenerated holes (h^+).

3. Experimental

3.1 Phase and morphology analysis synthetic procedures

Fig. 1a illustrates the XRD patterns and structural evolution of Bi_2WO_6-based catalysts. The pristine Bi_2WO_6 exhibits diffraction peaks at 28.4°, 32.6°, and 47.1°, corresponding to the (131), (060), and (102) planes of the orthorhombic phase (JCPDS #39-0256),[25,26] confirming its well-defined crystal structure. Upon Fe^{3+} doping, the (131) peak undergoes a low-angle shift of 0.15°, and the calculated interplanar spacing (*via* Bragg's law) increases due to lattice expansion induced by the isovalent substitution of W^{6+} (0.60 Å) by Fe^{3+} (0.64 Å) (Fig. 1b).

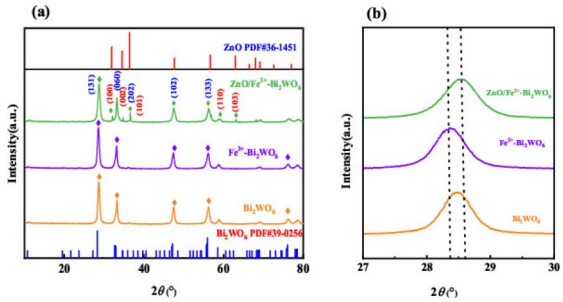

Fig. 1 XRD patterns of different catalysts (a) and partially enlarged XRD patterns (b).

Subsequent incorporation of ZnO introduces distinct peaks at 31.7°, 36.2°, and 56.6°, matching the wurtzite structure of ZnO (JCPDS #36-1451).[27,28] Notably, the (131) peak shifts back to higher angles with a broadened full width at half-maximum (FWHM), indicative of interfacial lattice strain at the ZnO/Fe^{3+}-doped Bi_2WO_6 heterojunctions. This strain effect, combined with Zn distribution (4.07 wt%) revealed by EDS elemental mapping, collectively validates the successful construction of the system.

Fig. 2 comparatively analyzes the morphological evolution of pristine Bi_2WO_6 and ZnO/Fe^{3+}-doped Bi_2WO_6 *via* SEM characterization. The unmodified Bi_2WO_6 exhibits a compact platelet morphology with an average lateral dimension of 0.5 μm (Fig. 2a–c). In stark contrast, the ZnO/Fe^{3+}-doped Bi_2WO_6 heterostructure demonstrates significantly expanded nanosheets (1–2 μm) featuring a fluffy architecture composed of interconnected ultrathin layers (Fig. 2d–f). The resultant hierarchical porous structure achieves a substantially enhanced specific surface area, which facilitates reactant molecule adsorption and maximizes exposure of catalytically active sites.

Fig. 3 systematically characterizes the microstructure and elemental distribution of the ZnO/Fe^{3+}-doped Bi_2WO_6 nanocomposites. The low-magnification TEM image (Fig. 3a) reveals, a translucent lamellar architecture with lateral dimensions of 1–2 μm consistent with the fluffy morphology observed by SEM. High-resolution TEM imaging (Fig. 3b–d) demonstrates that ultrathin ZnO nanosheets are uniformly anchored on the Bi_2WO_6 substrate, forming well-defined 2D heterointerfaces

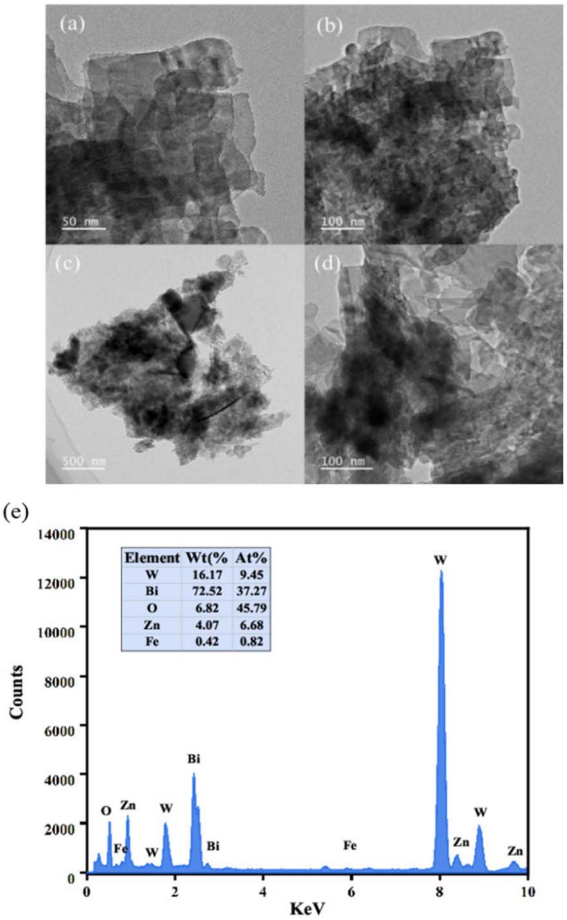

Fig. 3 TEM images of the ZnO/Fe^{3+}-doped Bi_2WO_6 nanocomposites (a–d) and TEM-EDS diagram (e).

through edge-contact interactions. The TEM-EDS elemental mapping (Fig. 3e) deciphers the spatial distribution characteristics: Bi and W exhibit continuous distributions across the basal planes, Zn displays edge-enriched patterns at the nanosheet peripheries, and Fe is homogeneously dispersed within the Bi_2WO_6 lattice. This multiscale structural consistency—spanning crystallographic features, morphological evolution, and elemental localization—conclusively validates the precision-engineered architecture.

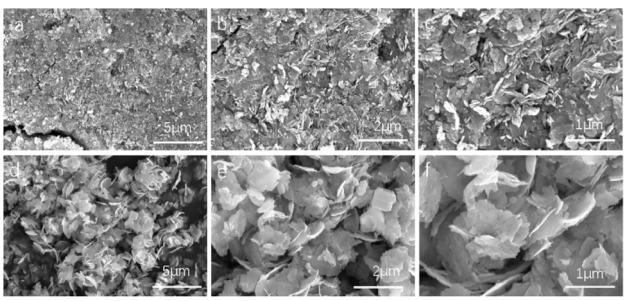

Fig. 2 SEM images of Bi_2WO_6 (a–c) and ZnO/Fe^{3+}-doped Bi_2WO_6 (d–f).

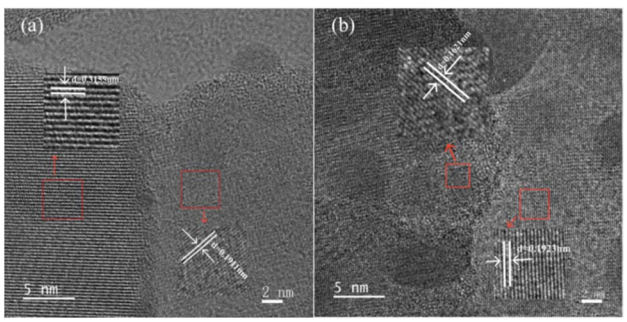

Fig. 4 TEM images of ZnO/Fe^{3+}-doped Bi_2WO_6 catalysts (a and b).

Fig. 4 reveals the atomic-scale interfacial characteristics of the ZnO/Fe^{3+}-doped Bi_2WO_6 heterojunction through high-resolution TEM (HRTEM) and STEM analyses. The TEM/SEM images clearly show nanoscale ZnO particles uniformly deposited on the surface of Fe^{3+}-doped Bi_2WO_6 nanosheets, forming defect-free and tightly bonded interfacial contacts (Fig. 4a and b). HRTEM analysis of the interfacial region (Fig. 4a) demonstrates a lattice spacing about 0.316 nm for Fe^{3+}-Bi_2WO_6, corresponding to the (131) plane of the orthorhombic Bi_2WO_6. This spacing exhibits lattice expansion compared to the undoped sample (0.315 nm), attributed to Fe^{3+}-induced lattice distortion. Adjacent to this, a spacing of 0.191 nm matches the (102) plane of wurtzite ZnO, indicating coherent lattice alignment between the two phases with no amorphous interfacial layers. Further interfacial analysis (Fig. 4b) reveals additional crystallographic features: 0.1621 nm and 0.1923 nm lattice spacings correspond to the ZnO (110) and Bi_2WO_6 (202) planes, respectively. These values show negligible deviation from standard reference data (JCPDS #39-0256 for Bi_2WO_6; JCPDS #36-1451 for ZnO), confirming the structural integrity of both phases. This provides direct evidence for the precisely constructed heterojunction, where ZnO nanoparticles establish strong electronic coupling with the Fe^{3+}-doped Bi_2WO_6 substrate. Such interfacial characteristics are critical for enabling efficient charge transfer during photocatalytic processes.

Fig. 5 systematically characterizes the surface chemical states and elemental coordination environments of the ZnO/Fe^{3+}-doped Bi_2WO_6 composite and Bi_2WO_6. The full-spectrum analysis (Fig. 5a) clearly detects characteristic signal peaks corresponding to five elements: Bi, W, O, Zn, and Fe, which are fully consistent with the designed material composition. The high-resolution Bi 4f spectrum (Fig. 5b) exhibits two typical peaks at 158.9 eV and 164.23 eV, assigned to the Bi^{3+} $4f_{7/2}$ and $4f_{5/2}$ orbitals, respectively.[29,30] The binding energy separation matches standard Bi_2WO_6, confirming the structural integrity of the Bi–O–W framework. It can be seen from the Bi 4f spectrum that the ZnO/Fe^{3+}-doped Bi_2WO_6 moves to a higher binding energy direction than Bi_2WO_6, which confirms the driven directional electron transfer along the Bi_2WO_6 → Fe^{3+} → ZnO path. It also reveals the synergistic effect of heterojunction engineering and ion doping in optimizing the electronic structure. The O 1s spectrum (Fig. 5c) is deconvoluted into three chemical states: the dominant peak at 529.73 eV corresponds to lattice oxygen (OL) in Bi_2WO_6, the secondary peak at 530.40 eV arises from oxygen vacancy defects (OV), and the higher binding energy peak at 531.61 eV originates from surface-adsorbed oxygen species (OA).[31–33] The relative intensity ratio (OV/OL = 0.15) indicates the presence of abundant active sites in the material and the concentration of oxygen vacancies is significantly higher than that of Bi_2WO_6. The Zn 2p spectrum (Fig. 5d) displays symmetric doublet peaks at 1021.86 eV (Zn $2p_{3/2}$) and 1044.91 eV ($2p_{1/2}$), with a spin-orbit splitting energy of 23.05 eV, which is fully consistent with Zn^{2+} characteristics, confirming the existence of ZnO as an independent phase.[29,34,35] In the W 4f spectrum (Fig. 5e), the characteristic peaks at 35.18 eV ($4f_{7/2}$) and 37.36 eV ($4f_{5/2}$) verify the stable presence of W^{6+}.[29,36] The absence of significant peak broadening demonstrates that Fe^{3+} doping does not disrupt the WO_6 octahedral structure. Notably, the Fe 2p spectrum (Fig. 5f) exhibits characteristic peaks at 712.31 eV ($2p_{3/2}$) and 724.68 eV ($2p_{1/2}$), confirming the successful incorporation of Fe^{3+}.[33,37] These results mutually corroborate the successful construction of the ZnO/Fe^{3+}-doped Bi_2WO_6 system.

Fig. 6 systematically elucidates the pore topology and mass transfer enhancement mechanisms of the ZnO/Fe^{3+}-doped Bi_2WO_6 nanocomposite. The N_2 adsorption–desorption isotherm (Fig. 6) exhibits Type IV characteristics with an H3-type hysteresis loop, consistent with slit-shaped pores in layered materials, aligning with TEM-observed stacked

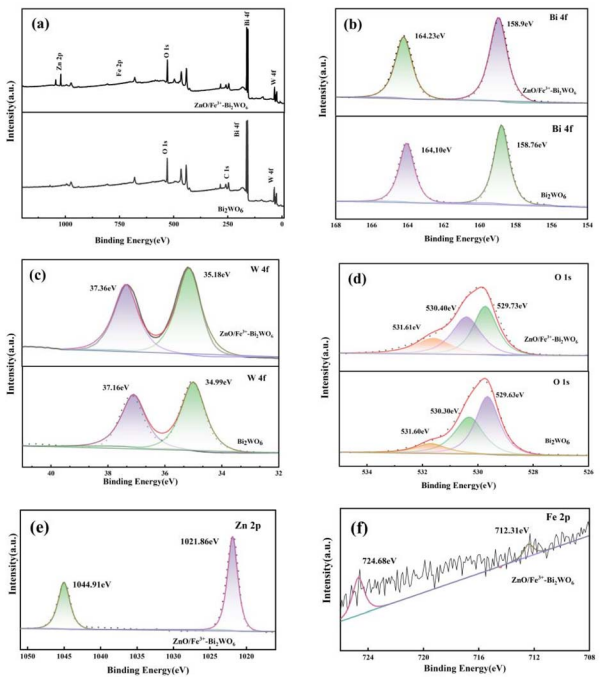

Fig. 5 XPS spectra of ZnO/Fe^{3+}-doped Bi_2WO_6 and Bi_2WO_6 sample: (a) survey of the photocatalyst; (b) Bi 4f; (c) W 4f; (d) O 1s; (e) Zn 2p; (f) Fe 2p.

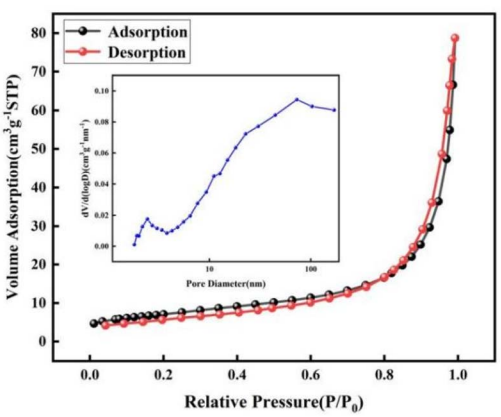

Fig. 6 Nitrogen adsorption–desorption isotherm, and pore size distribution of ZnO/Fe^{3+}-doped Bi_2WO_6.

nanosheets. The BJH pore size distribution curve (Fig. 6) reveals a bimodal pore structure: a dominant peak at 23.02 nm (mesoporous region, 2–50 nm) and a secondary peak extending to 72.5 nm (macropore region, >50 nm). This hierarchical architecture originates from Fe^{3+} doping-induced lattice strain and ZnO heterointerface engineering.

The BET specific surface area (25.2 $m^2\ g^{-1}$) shows a 26% enhancement compared to pristine Bi_2WO_6 (literature value about 20 $m^2\ g^{-1}$ (ref. 38–40)), with a total pore volume of 0.1221 $cm^3\ g^{-1}$, where mesopores account for half of the total pore volume. Microstrain induced by lattice distortion expands the interlayer spacing of Bi_2WO_6, while the spatial confinement effect of ZnO nanosheets suppresses dense stacking of layered plates. These synergistic interactions create an interconnected pore network. This unique structure endows the material with dual mass transfer advantages: (1) mesopores enhance tetracycline (TC) molecule enrichment *via* Kelvin capillary condensation, significantly increasing local concentration; (2) macropores serve as rapid mass transfer channels, substantially improving molecular diffusion rates.

Fig. 7 provides an in-depth analysis of the chemical bonding and defect evolution mechanisms at the ZnO/Fe^{3+}-doped Bi_2WO_6 heterointerface through Fourier-transform infrared spectroscopy (FT-IR). The calcined sample exhibits a prominent absorption peak at 1300 cm^{-1} (Fig. 7), attributed to oxygen vacancies (VO) 3.2 associated with metal-oxygen lattice vibrations. The peak intensity increases significantly after calcination, combined with XPS quantification, confirming that high-temperature treatment induces oxygen deintercalation from the Bi_2WO_6 lattice, generating high-concentration VO defects.[41,42] Gaussian peak deconvolution of the 1450 cm^{-1} feature resolves two components: a broadened peak at 1428 cm^{-1} corresponding to the δ(Zn–O) bending vibration in the ZnO lattice, and a shoulder peak at 1465 cm^{-1} originating from ν(Zn–O–W) heterointerface vibrations.[43,44] This unique vibrational mode provides direct spectroscopic evidence of chemical bonding between ZnO and Bi_2WO_6. Spectral evolution analysis reveals critical structural changes: the disappearance of the adsorbed water hydroxyl (–OH) peak (1380 cm^{-1}) indicates enhanced crystallinity, while the concurrent enhancement of VO defect peaks and ν(Zn–O–W) vibrational peaks confirms that the heterointerface achieves atomic-level bonding *via* solid-phase reaction.[45]

3.2 Optical analysis

Fig. 8 reveals the synergistic light-harvesting enhancement mechanism of ZnO/Fe^{3+}-doped Bi_2WO_6 through UV-vis diffuse reflectance spectroscopy (UV-DRS) and multiscale band engineering theory. As shown in Fig. 8a, the composite exhibits a significant red shift in absorption edge to 480 nm, extending its visible-light response range by 30 nm, 80 nm, and 30 nm compared to pristine Bi_2WO_6 (450 nm), ZnO (400 nm),and the Fe^{3+}-doped sample (0.26Fe^{3+}-Bi_2WO_6, 450 nm), respectively. This broadening of absorption arises from dual regulatory effects: (1) Fe^{3+} doping introduces intermediate 3d-orbital energy levels below the conduction band of Bi_2WO_6; (2) heterojunction formation between ZnO ($E_g = 3.20$ eV) and Fe^{3+}-doped Bi_2WO_6 ($E_g = 2.89$ eV), where the built-in electric field (0.57 V, confirmed by Mott–Schottky measurements) reduces the apparent bandgap to 2.68 eV *via* band bending effects, demonstrating a non-additive reduction.

According to Tauc's eqn (2), the bandgaps of ZnO and Bi_2WO_6 are estimated based on their UV-vis DRS spectra (Fig. 8b). Here, α denotes the light absorption coefficient, h represents Planck's constant, ν denotes the light frequency, A is a proportionality constant, and n are the band energy and E_g signifies the bandgap energy. ZnO and Bi_2WO_6 are indirect semiconductors, so n is 1/2.

$$\alpha h\nu = A(h\nu - E_g)^{n/2} \quad (2)$$

The composite material exhibits a bandgap of 2.68 eV, which is 0.30 eV narrower than pristine Bi_2WO_6 (2.98 eV) and significantly lower than the Fe^{3+}-doped system (2.89 eV). These results confirm the synergistic interplay between heterojunction engineering and ion doping in optimizing electronic structures.

Fig. 9 elucidates the charge separation enhancement mechanism of ZnO/Fe^{3+}-doped Bi_2WO_6 through steady-state photoluminescence (PL) spectroscopy and carrier dynamics analysis. Under 470 nm laser excitation (matching the band-edge transition energy of Bi_2WO_6), the PL emission intensity of the composite is significantly reduced compared to pristine Bi_2WO_6, indicating effective suppression of non-radiative

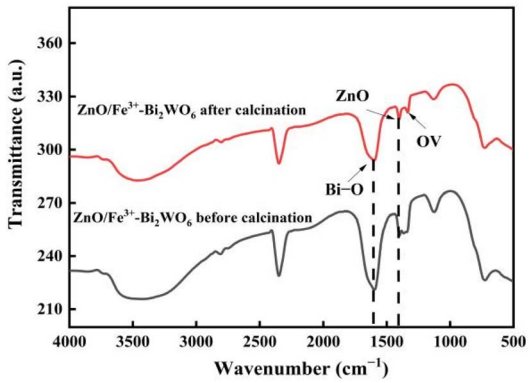

Fig. 7 Infrared spectra of ZnO/Fe^{3+}-doped Bi_2WO_6 before and after calcination.

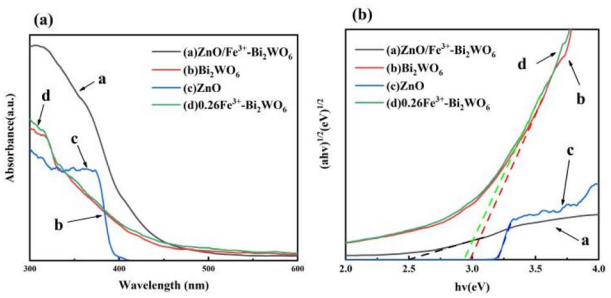

Fig. 8 UV diffuse reflection spectra of different photocatalytic materials (a) and band gap (b).

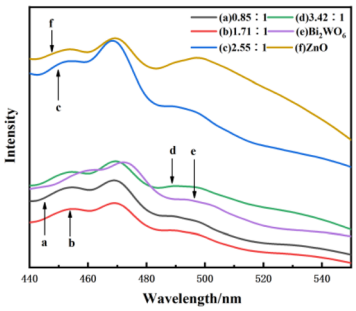

Fig. 9 Fluorescence spectra of ZnO/Fe^{3+}-doped Bi_2WO_6, pure Bi_2WO_6 and ZnO with different molar ratios.

carrier recombination pathways. Combined Mott–Schottky measurements and HRTEM interfacial analysis reveal that a flat-band potential shift ($\Delta E_{fb} = 0.57$ eV) at the heterojunction interface induces a built-in electric field. This field drives directional electron migration along the Bi_2WO_6 → Fe^{3+} → ZnO transfer pathway. The synergy between defect-state trapping and charge transfer mechanisms significantly enhances photocatalytic degradation under visible light.

3.3 Electrical properties

Fig. 10a and b systematically elucidates the charge transport dynamics enhancement mechanism of the ZnO/Fe^{3+}-doped Bi_2WO_6 heterojunction through electrochemical impedance spectroscopy (EIS) and transient photocurrent response (TPR) techniques. The Nyquist plot reveals a significantly smaller semicircular arc radius for the composite compared to pristine Bi_2WO_6 and ZnO, indicating markedly reduced interfacial charge transfer resistance, a breakthrough attributed to the synergistic interplay between Fe^{3+} doping and heterojunction

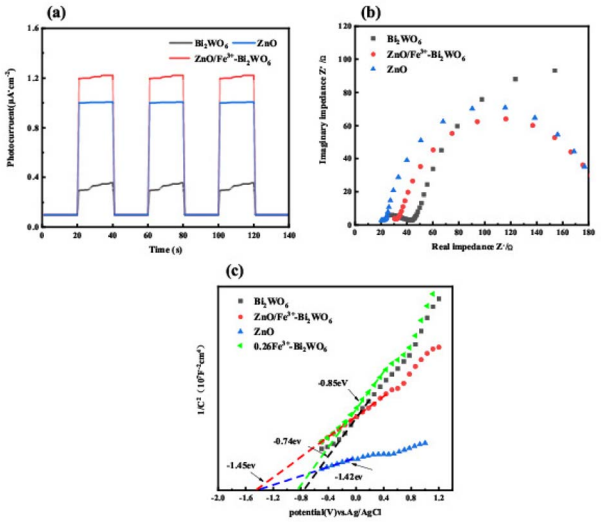

Fig. 10 Impedance spectra (a), photocurrent response curves (b) and MS curves (c) of ZnO/Fe^{3+}-doped Bi_2WO_6, Bi_2WO_6, ZnO and 0.26Fe^{3+}-doped Bi_2WO_6.

engineering. Mott–Schottky measurements combined with HRTEM interfacial analysis demonstrate that the flat-band potential shift at the heterojunction interface induces a built-in electric field, which drives directional migration of photogenerated electrons along the Fe^{3+}-Bi_2WO_6 → ZnO → electrolyte pathway. TPR testing further confirms that the composite achieves a photocurrent density of 1.246 mA cm^{-2} under illumination, representing 3.5-fold and 1.23-fold enhancements over pristine Bi_2WO_6 and ZnO, respectively. This performance breakthrough stems from the dual synergistic mechanisms of "band alignment-defect bridge": the gradient band structure of the heterojunction enables efficient charge separation, while Fe^{3+}-induced oxygen vacancies (OV/OL = 0.15) act as electron relay stations to accelerate interfacial charge transfer. These innovations together greatly improve the photocatalytic performance, establishing a new benchmark for similar materials.

As shown in Fig. 10(c), the curves of ZnO/Fe^{3+}-doped Bi_2WO_6, Bi_2WO_6, ZnO and 0.26Fe^{3+}-doped Bi_2WO_6 all show positive slope characteristics in the test potential range (−2.0 to 0.2 V *vs.* SCE), which strictly conforms to the classical response behavior of n-type semiconductors. The flat band potentials of ZnO/Fe^{3+}-doped Bi_2WO_6 (−1.45 eV), Bi_2WO_6 (−0.74 eV), ZnO (−1.42 eV) and 0.26Fe^{3+}-doped Bi_2WO_6 (−0.85 eV) were determined by linear extrapolation method. It must be taken into account that their flat band potential (E_{fb}) is −1.45 V (−1.25 V *vs.* NHE), −0.74 V (−0.54 V *vs.* NHE), −1.42 V (−1.22 V *vs.* NHE), −0.85 V (−0.65 V *vs.* NHE) relative to the Ag/AgCl distribution.[46] The numerical differences reflect band engineering modulation.

According to semiconductor electrochemistry theory, the relationship between E_{fb} and conduction band minimum (E_{CB}) for n-type semiconductors is: $E_{CB} = E_{fb} - 0.1$ eV (pH = 7).[46,47] Therefore, the E_{CB} of 0.26Fe^{3+}-doped Bi_2WO_6 is −0.75 eV, and that of ZnO is −1.32 eV. The E_{fb} of 0.26Fe^{3+}-doped Bi_2WO_6 is negatively shifted by 0.11 eV compared with that of pure Bi_2WO_6, indicating that the substitution of Fe^{3+} for W^{6+} sites induces the formation of oxygen vacancies. The E_{fb} of ZnO/Fe^{3+}-doped Bi_2WO_6 is further negatively shifted by 0.60 eV due to the dual effects of the built-in electric field and the space charge layer reconstruction.

3.4 Photocatalytic activity test

Fig. 11 systematically elucidates the photocatalytic performance enhancement mechanism and degradation kinetics of the ZnO/Fe^{3+}-doped Bi_2WO_6 heterojunction. Under simulated sunlight irradiation, the Fe^{3+}-doped sample (0.26Fe^{3+}-Bi_2WO_6) achieves a tetracycline (TC) degradation efficiency of 80.09% within 60 minutes (Fig. 11a), representing a 19.99 percentage point improvement over pristine Bi_2WO_6 (60.1%).

This performance breakthrough originates from Fe^{3+} doping-induced oxygen vacancy concentration enhancement (XPS quantification: OV/OL = 0.15). Upon constructing the ZnO heterojunction (mass ratio 1.71 : 1), the degradation efficiency surges to 95.5% (Fig. 11b), with a reaction rate constant (k) of 0.05343 min^{-1} (Fig. 11d), which is 2.28-fold higher than that of Fe^{3+}-doped Bi_2WO_6 (0.02344 min^{-1}) and 2.7-fold greater than

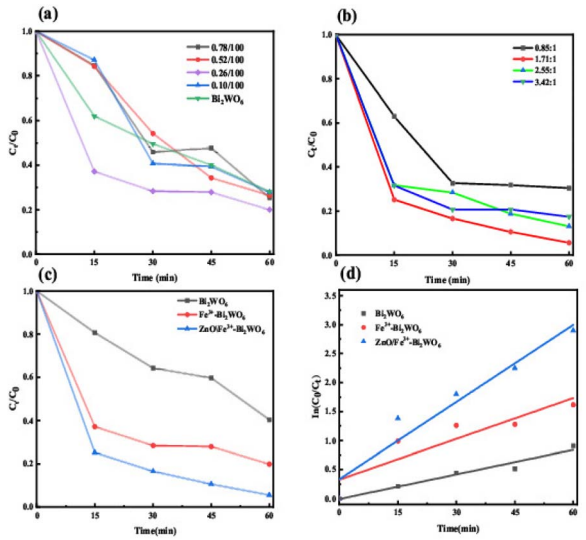

Fig. 11 Degradation curves (a–c) and kinetic curves (d) of different materials under simulated sunlight irradiation.

pristine Bi_2WO_6 (0.01983 min^{-1}), establishing it as one of the highest reported values among similar materials.

The performance improvement is attributed to the triple synergy mechanism: (1) heterojunction interface engineering: HRTEM and SAED analysis show that ZnO nanosheets (thickness 8 nm) form a coherent interface with Bi_2WO_6 through edge contact, and the Mott–Schottky test shows that the interface generates a certain intensity of built-in electric field ($\Delta E_{fb} = 0.57$ eV); (2) synergistic effect of defect states: Fe^{3+} replaced W site to cause lattice distortion; (3) multi-stage mass transfer channels: BET analysis showed that the hierarchical pore structure (mesoporous 23 nm, macroporous 72.5 nm) significantly increased the diffusion rate of TC molecules, and finally achieved a breakthrough improvement in photocatalytic performance.

Fig. 12a evaluates the cycling stability of the ZnO/Fe^{3+}-doped Bi_2WO_6 heterojunction. Over five consecutive cycles, the TC degradation efficiency remains at 95.5%, 92.65%, 90.09%, 89.96%, and 87.89%, with a cumulative decay of only 7.61 percentage points, demonstrating exceptional structural durability. This stability arises from the lattice reinforcement, and

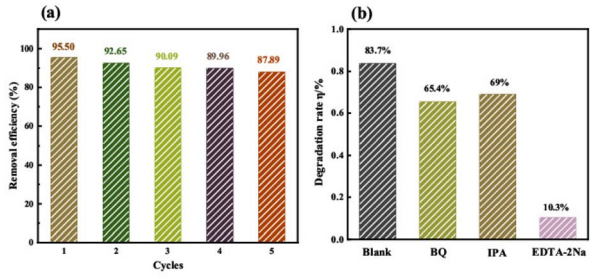

Fig. 12 The cycle experimental diagram (a) and active species capture experimental diagram (b) of ZnO/Fe^{3+}-Bi_2WO_6 catalyst.

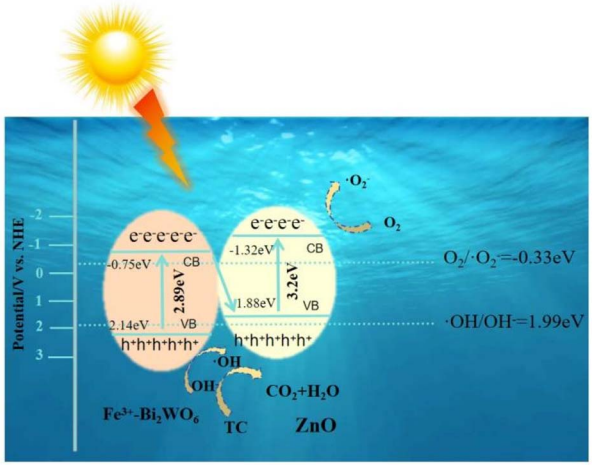

Fig. 13 Degradation mechanism of ZnO/Fe^{3+}-doped Bi_2WO_6.

pore preservation mechanisms, highlighting its potential for industrial applications in complex aqueous environments.

Fig. 12b reveals the dominant active species *via* radical trapping experiments. Under the addition of scavengers for $\cdot O_2^-$ (BQ), ·OH (IPA), and h^+ (EDTA-2Na), the tetracycline degradation rates decreased to 65.4%, 69%, and 10.3%, respectively, confirming photogenerated holes (h^+) as the primary drivers of degradation.

3.5 Mechanism analysis

Fig. 13 elucidates the charge transfer mechanism in the ZnO/Fe^{3+}-doped Bi_2WO_6 heterojunction through band engineering and spectroscopic characterization techniques. Mott–Schottky tests combined with UV-vis analysis reveal that ZnO and Fe^{3+}-doped Bi_2WO_6 form a built-in electric field of 0.57 eV (ΔE_{fb} = 0.57 eV) at their interface, with conduction band (CB) positions at −1.32 eV and −0.75 eV, respectively. Based on Equation:

$$E_{VB} = E_g + E_{CB} \quad (3)$$

The valence band (VB) are calculated as 1.88 eV and 2.14 eV.[48] The built-in field drives the photogenerated electrons to migrate from the CB of Fe^{3+}-doped Bi_2WO_6 to the VB of ZnO, which effectively separates the carriers and reduces the recombination of photogenerated carriers. The photogenerated e^- with stronger reduction ability on the CB of ZnO and the strong oxidation ability h^+ of VB of Bi_2WO_6 are retained, forming a unique Z-type charge transfer pathway (Fig. 13).

In contrast, a conventional Type-II heterojunction—where electrons from the CB of Fe^{3+}-doped Bi_2WO_6 would migrate to the VB of ZnO—is limited by the insufficient oxidation capacity of ZnO's VB holes (1.88 eV *vs.* the ·OH/$\cdot OH^-$ oxidation potential of 1.99 eV). This contradicts scavenger experiments and fails to achieve efficient degradation. The Z-scheme system, however, enables effective separation of photogenerated electrons and holes, resulting in a tetracycline degradation rate constant of 0.5343 min^{-1} and highly efficient degradation.

4. Conclusions

This study constructed a Z-scheme ZnO/Fe^{3+}-Bi_2WO_6 photocatalytic system through synergistic integration of Fe^{3+} doping and ZnO heterostructure for efficient tetracycline degradation. The research demonstrated that Fe^{3+} lattice doping combined with ZnO heterointerface engineering formed a hierarchical porous structure, extending visible light absorption to 480 nm with a bandgap reduction of 0.30 eV. The built-in electric field at the Z-type heterogeneous interface promotes the effective separation of charges. Experiments confirm that h^+ is the main active species, and the system exhibits high carrier separation efficiency and cycle stability. Optimal component ratios (ZnO : Bi_2WO_6 : Fe^{3+} = 1.71 : 1 : 0.26) achieved dynamic equilibrium among photon capture, charge transfer kinetics, and surface redox processes, enabling 95.5% tetracycline removal within 60 min ($k = 0.052\ min^{-1}$). This work proposes a "defect regulation-heterostructure" integrated strategy, providing theoretical insights for designing bismuth-based Z-scheme photocatalysts and demonstrates potential applicability in antibiotic wastewater treatment.

Data availability

The data that support the findings of this study are available from the corresponding author upon reasonable request.

Author contributions

Hui Sun: supervision, validation, writing – original draft, software; Gaoyang Liang: methodology, software; Bingge Chen: software, investigation; Jingqi Jia: visualization, software; Hongxia Jing: conceptualization, data curation, funding acquisition, writing – review & editing.

Conflicts of interest

The authors declare no competing financial interest.

Acknowledgements

This work was supported by Fundamental Research Program of Shanxi Province (No. 202203021212137).

Notes and references

1 Y. Amangelsin, Y. Semenova, M. Dadar, M. Aljofan and G. Bjorklund, *Antibiotics*, 2023, **12**, 440.
2 A. Balakrishnan, M. Chinthala, R. K. Polagani and D. V. N. Vo, *Environ. Res.*, 2023, **216**, 114660.
3 H. Liu, W. C. Huo, T. C. Zhang, L. Ouyang and S. J. Yuan, *Mater. Today Chem.*, 2022, **23**, 100729.
4 A. Fiaz, D. C. Zhu and J. Z. Sun, *Environ. Sci. Eur.*, 2021, **33**, 64.
5 F. Nguyen, A. L. Starosta, S. Arenz, D. Sohmen, A. Dönhöfer and D. N. Wilson, *Biol. Chem.*, 2014, **395**, 559–575.
6 X. N. Wang, J. P. Jia and Y. L. Wang, *Chem. Eng. J.*, 2017, **315**, 274–282.
7 M. Ahmadi, H. R. Motlagh, N. Jaafarzadeh, A. Mostoufi, R. Saeedi, G. Barzegar and S. Jorfi, *J. Environ. Manage.*, 2017, **186**, 55–63.
8 Y. J. Dai, M. Liu, J. J. Li, S. S. Yang, Y. Sun, Q. Y. Sun, W. S. Wang, L. Lu, K. X. Zhang, J. Y. Xu, W. L. Zheng, Z. Y. Hu, Y. H. Yang, Y. W. Gao and Z. H. Liu, *Sep. Sci. Technol.*, 2020, **55**, 1005–1021.
9 D. B. Wang, F. Y. Jia, H. Wang, F. Chen, Y. Fang, W. B. Dong, G. M. Zeng, X. M. Li, Q. Yang and X. Z. Yuan, *J. Colloid Interface Sci.*, 2018, **519**, 273–284.
10 U. Ewuzie, O. D. Saliu, K. Dulta, S. Ogunniyi, A. O. Bajehg, K. O. Iwuozori and J. O. Ighaloj, *J. Water Proc. Eng.*, 2022, **50**, 103273.
11 F. B. Zhang, X. M. Wang, H. N. Liu, C. L. Liu, Y. Wan, Y. Z. Long and Z. Y. Cai, *Appl. Sci.*, 2019, **9**, 2489.
12 G. J. Wang, S. S. Lv, Y. H. Shen, W. Li, L. H. Lin and Z. C. Li, *J Mater.*, 2024, **10**, 315–338.
13 T. Chen, L. Z. Liu, C. Hu and H. W. Huang, *Chin. J. Catal.*, 2021, **42**, 1413–1438.
14 P. Ju, P. Wang, B. Li, H. Fan, S. Y. Ai, D. Zhang and Y. Wang, *Chem. Eng. J.*, 2014, **236**, 430–437.
15 Y. Y. Zhu, Y. J. Wang, Q. Ling and Y. F. Zhu, *Appl. Catal., B*, 2017, **200**, 222–229.
16 B. S. Li, C. Lai, G. M. Zeng, L. Qin, H. Yi, D. L. Huang, C. Y. Zhou, X. G. Liu, M. Cheng, P. Xu, C. Zhang, F. L. Huang and S. Y. Liu, *ACS Appl. Mater. Interfaces*, 2018, **10**, 18824–18836.
17 S. J. Li, M. J. Cai, Y. P. Liu, J. L. Zhang, C. C. Wang, S. H. Zang, Y. J. Li, P. Zhang and X. Li, *Inorg. Chem. Front.*, 2022, **9**, 2479–2497.
18 Z. L. Guan, X. M. Li, Y. Wu, Z. Chen, X. D. Huang, D. B. Wang, Q. Yang, J. L. Liu, S. H. Tian, X. Y. Chen and H. Zhao, *Chem. Eng. J.*, 2021, **410**, 128283.
19 J. Sun, C. H. Shen, J. Guo, H. Guo, Y. F. Yin, X. J. Xu, Z. H. Fei, Z. T. Liu and X. J. Wen, *J. Colloid Interface Sci.*, 2021, **588**, 19–30.
20 Z. Liu, X. Q. Liu, L. F. Wei, C. L. Yu, J. H. Yi and H. B. Ji, *Appl. Surf. Sci.*, 2020, **508**, 145309.
21 Y. Zhang, C. Chai, X. C. Zhang, J. X. Liu, D. H. Duan, C. M. Fan and Y. F. Wang, *Inorg. Chem. Commun.*, 2019, **100**, 81–91.
22 M. Q. Du, S. X. Cao, X. Z. Ye and J. F. Ye, *J. Nanosci. Nanotechnol.*, 2020, **20**, 5861–5873.
23 L. Schumacher and R. Marschall, *Top. Curr. Chem.*, 2022, **380**, 53.
24 D. Liu, S. T. Chen, R. J. Li and T. Y. Peng, *Acta Phys.-Chim. Sin.*, 2021, **37**, 2010017.
25 J. J. Ma, L. Tian, C. Xu, Y. M. Zhang, T. Zhang, H. X. Li, P. F. Zhao, Y. Q. Liang, J. W. Wang and X. X. Fan, *Catal. Lett.*, 2018, **148**, 41–50.
26 Z. Li, X. M. Zhu, Y. Liu, H. Liu and B. Sun, *Environ. Sci. Pollut. Res.*, 2022, **29**, 69785–69797.
27 K. Chaudhary, N. Shaheen, S. Zulfiqar, M. I. Sarwar, M. Suleman, P. O. Agboola, I. Shakir and M. F. Warsi, *Synth. Met.*, 2020, **269**, 116526.

28 S. Rajendran, M. M. Khan, F. Gracia, J. Q. Qin, V. K. Gupta and S. Arumainathan, *Sci. Rep.*, 2016, **6**, 31641.
29 R. Radha, R. V. Kulangara, E. Elaiyappillai, J. Sridevi and S. Balakumar, *Cryst. Growth Des.*, 2019, **19**, 6224–6238.
30 G. Y. Long, J. F. Ding, L. H. Xie, R. Z. Sun, M. X. Chen, Y. F. Zhou, X. Y. Huang, G. R. Han, Y. J. Li and W. R. Zhao, *Appl. Surf. Sci.*, 2018, **455**, 1010–1018.
31 H. Q. Jiang, Q. An and S. Y. Zang, *J. Environ. Chem. Eng.*, 2023, **11**, 110960.
32 D. H. Liu, L. L. Wu, Z. H. Su, J. Liu, L. L. Feng and J. F. Huang, *Catal. Commun.*, 2023, **183**, 106760.
33 X. X. Deng, S. Tian, Z. M. Chai, Z. J. Bai, Y. X. Tan, L. Chen, J. K. Guo, S. Shen, M. Q. Cai, C. T. Au and S. F. Yin, *Ind. Eng. Chem. Res.*, 2020, **59**, 13528–13538.
34 J. H. Luo, K. Zhang, M. L. Cheng, M. M. Gu and X. K. Sun, *Chem. Eng. J.*, 2020, **380**, 122625.
35 J. Cheng, Y. Shen, K. Chen, X. Wang, Y. F. Guo, X. J. Zhou and R. B. Bai, *Chin. J. Catal.*, 2018, **39**, 810–820.
36 T. Fei, L. M. Yu, Z. Y. Liu, Y. H. Song, F. Xu, Z. Mo, C. B. Liu, J. J. Deng, H. Y. Ji, M. Cheng, Y. C. Lei, H. Xu and H. M. Li, *J. Colloid Interface Sci.*, 2019, **557**, 498–505.
37 D. J. Wang, L. L. Yue, L. Guo, J. Zhang, F. Fu and G. L. Xue, *Chin. J. Inorg. Chem.*, 2014, **30**, 961–968.
38 H. Y. Jiang, J. H. He, C. Y. Deng, X. D. Hong and B. Liang, *Molecules*, 2022, **27**, 8698.
39 X. D. Zhu, F. Q. Qin, X. P. Zhang, Y. Y. Zhong, J. Wang, Y. Jiao, Y. H. Luo and W. Feng, *Int. J. Mol. Sci.*, 2022, **23**, 8422.
40 J. Wang, X. D. Zhu, F. Q. Qin, Y. X. Wang, Y. Sun and W. Feng, *Mater. Lett.*, 2022, **314**, 131892.
41 W. An, S. M. Wang, Y. Fu, Y. Guan, Z. Y. Li, T. Xu and H. R. Wang, *Desalin. Water Treat.*, 2021, **216**, 151–161.
42 D. Y. Peng, H. Y. Zeng, J. Xiong, F. Y. Liu, L. H. Wang, S. Xu, Z. L. Yang and S. G. Liu, *J. Colloid Interface Sci.*, 2023, **629**, 133–146.
43 J. Wang, R. S. Chen, L. Xiang and S. Komarneni, *Ceram. Int.*, 2018, **44**, 7357–7377.
44 Z. G. Geng, X. D. Kong, W. W. Chen, H. Y. Su, Y. Liu, F. Cai, G. X. Wang and J. Zeng, *Angew. Chem., Int. Ed.*, 2018, **57**, 6054–6059.
45 Y. Liu, B. Wei, L. L. Xu, H. Gao and M. Y. Zhang, *Chemcatchem*, 2015, **7**, 4076–4084.
46 A. Phuruangrat, P. Dumrongrojthanath, T. Thongtem and S. Thongtem, *J. Ceram. Soc. Jpn.*, 2017, **125**, 500–503.
47 S. Pinchujit, A. Phuruangrat, S. Wannapop, T. Sakhon, B. Kuntalue, T. Thongtem and S. Thongtem, *Russ. J. Inorg. Chem.*, 2022, **67**, S199–S209.
48 P. Kumar, S. Verma, N. C. Korosin, B. Zener and U. L. Stangar, *Catal. Today*, 2022, **397**, 278–285.